Maeng et al. *NPG Asia Materials* (2021)13:75
https://doi.org/10.1038/s41427-021-00343-7

NPG Asia Materials

ARTICLE Open Access

Unusual terahertz-wave absorptions in δ/α-mixed-phase $FAPbI_3$ single crystals: interfacial phonon vibration modes

Inhee Maeng[1], Seungjun Lee[2], E. Q. Han[3], Yurou Zhang[3], Seung Jae Oh[1], Masakazu Nakamura[4], Jung-Ho Yun[3], Lianzhou Wang[3], Young-Kyun Kwon[2,5] and Min-Cherl Jung[6]

Abstract

The terahertz (THz)-wave absorption properties in organic-inorganic hybrid perovskite (OHP) materials are investigated with the in-depth development of OHP-based THz applications. In the THz range from 0.5 to 3 THz, OHPs typically show several interesting phonon modes such as transverse, longitudinal, and halogen self-vibrations. To modulate these frequencies, the density changes in defect-incorporated structures and element mixtures were tested and confirmed. In the literature, the origin of phonon modes in OHP materials have been mostly explained. However, we found new phonon vibration modes in formamidinium (FA)-based hybrid perovskite structures. $FAPbI_3$ single crystals, organic–inorganic hybrid perovskites, of the δ-, δ/α-mixed-, and α-phases were prepared. We intriguingly found that the δ/α-mixed-phase exhibited significant THz-wave absorption peaks at 2.0 and 2.2 THz that were not related to any phonon modes from either the δ- or α-phases, although the δ/α-mixed-phase sample was confirmed to be formed by a physical combination of the δ- and α-phases without the creation of any new chemical states. Our theoretical study performed with ab initio calculations provides an explanation for these unusual THz-wave absorption behaviors; they originate from the novel vibration modes excited at the seamless interfaces in the mixed phase of $FAPbI_3$.

Introduction

Organic–inorganic hybrid perovskite (OHP) materials with universal physical properties, such as controllable bandgaps, weak exciton binding energies, and high-carrier mobilities with long lifetimes, are reviewed in terms of one of the challenges for several key applications including solar cells, optoelectronics, diodes, memory devices, and detectors[1–10]. Currently, the terahertz (THz) detector, one of the possible applications, has been a focus of attention because of its potential use in medical devices[9,11–16]. The THz energy range is strongly correlated with molecules and biomaterials[17–19]. In fact, OHP materials possess both molecular vibrations from the organic component and lattice vibrations from the inorganic component. Previous studies have shown that THz absorption depends not only on the elements comprising the perovskite but also on the corresponding fabrication methods[20–22]. Additionally, these materials have major advantages, including their low unit cost in comparison with that of highly purified III–V or II–VI compound semiconductor materials[23,24].

To realize THz-based applications using OHP materials, an in-depth understanding of phonon modes in the range of 0.5–3 THz is required. There have been several studies reporting the phonon characteristics of methylammonium (CH_3NH_3, MA)-based hybrid perovskites[9,11,14,25–27]. In short, three major phonon vibration modes, transverse (0.8–1.0 THz)/longitudinal (1.4–2.0 THz) vibrations from metal cation–halogen anion bonding and halogen self-vibrations (~2.0 THz), were found, and their origins were

Correspondence: Young-Kyun Kwon (ykkwon@khu.ac.kr) or Min-Cherl Jung (jung.mincherl.fp@u.tsukuba.ac.jp)
[1]YUHS-KRIBB, Medical Convergence Research Institute, College of Medicine, Yonsei University, Seoul, Republic of Korea
[2]Department of Physics, Kyung Hee University, Seoul, Republic of Korea
Full list of author information is available at the end of the article
These authors contributed equally: Inhee Maeng, Seungjun Lee

explained[9,11,14,25–27]. Additionally, significant THz-wave absorption at 1.58 THz due to a defect-incorporated hybrid perovskite structure was observed in $MAPbI_3$ fabricated by the sequential vacuum evaporation (SVE) method[6,11]. The THz-wave absorption properties of MA-based hybrid perovskite materials are mostly understood, and some applications such as sensors have been realized[9,11,14,25–27].

However, no studies have been published on the phonon properties of formamidinium-lead iodide, $[HC(NH_2)_2]PbI_3$ ($FAPbI_3$), because it typically contains two different phases, namely, the δ- and α-phases[28,29]. FA-based hybrid perovskite is more stable than MA-based hybrid perovskite[30] and constitutes a reasonable candidate for THz-based applications. In our previous research, we identified significant THz-wave absorption at 1.6 THz in the δ/α-mixed-phase in polycrystalline $FAPbI_3$ thin films[13]. This could have several possible origins, such as a structural defect at grain interfaces or small grain effects induced by the sequential vacuum evaporation method[12]. However, the physical origin of this significant THz-wave absorption has not been clearly identified because the polycrystalline phase has a number of degrees of freedom. A study with a single crystal must be performed to minimize the degrees of freedom.

Herein, we report our study on $FAPbI_3$ single crystals (SCs) of three different phases, the δ-, δ/α-mixed-, and α-phases, formed by post-annealing. In addition to basic characterizations for identifying atomic structures, surface morphology, and chemical states, we performed THz time-domain spectroscopy (THz-TDS) experiments and theoretical calculations to investigate the significant THz-wave absorption in the δ/α-mixed-phase. Interestingly, we found two unusual THz-wave absorptions at 2.0 and 2.2 THz that did not originate from either the δ- or α-phase. We revealed that the unusual THz-wave absorptions observed in the δ/α-mixed-phase originated from the interfacial phonon vibration modes at seamless interfaces in the mixed phase of $FAPbI_3$, although the δ/α-mixed-phase does not exhibit any chemical states different from those of either the δ- or α-phases. In this study, we confirm new findings of phonon vibration modes with different origins in OHP materials.

Materials and methods

PbI_2 (99%, Sigma–Aldrich, City, State, Country) and formamidinium iodide (FAI, 99.99%, Greatcell Solar) at the same molar ratio (1 M) were dissolved in 5 mL of gamma-butyrolactone (GBL, 99%, Sigma–Aldrich) to prepare the precursor solution. The solution was then filtered through a 0.45 μm polytetrafluoroethylene (PTFE) filter before crystallization. The vial that contained the precursor was placed in an oil bath, and its temperature was gradually increased to 120 °C at a rate of 1 °C/min. The vial was not disturbed for 6 h. Small SCs were harvested. Regularly shaped crystals were used as seeds to repeatedly grow in the fresh precursor to obtain larger sizes. Crystals were picked out and gently cleaned with Kimberly–Clark Kim wipes to remove solution residue. Later, the crystals were dried in an oven at 60 °C overnight. The entire process was performed in the air. To form each atomic structure such as the δ/α-mixed or α-phase, the as-received SC was annealed at 140 and 180 °C for 30 min in a N_2 glovebox (Fig. 1a–c).

To characterize each treated SC at various annealing temperatures, we performed X-ray diffraction (XRD), scanning electron microscopy (SEM), and high-resolution X-ray photoelectron spectroscopy (XPS). The XRD instrument was a RINT-TTRIII/NM with a Cu K_α source constructed by Rigaku. The SEM instrument was a HITACHI SU9000, and characterization was conducted at an acceleration voltage of 5 keV and an emission current of 10 μA. A VersaProbe II with monochromated Al K_α (ULVAC-PHI) was used for all XPS measurements to obtain Pb 4*f* and I 4*d* core-level and valence peaks. No trace of the O 1*s* core-level peak was observed in any treated states. The binding energies were calibrated with respect to the Au $4f_{7/2}$ level (84.0 eV)[31]. The THz conductivities of the $FAPbI_3$ SC were acquired by the

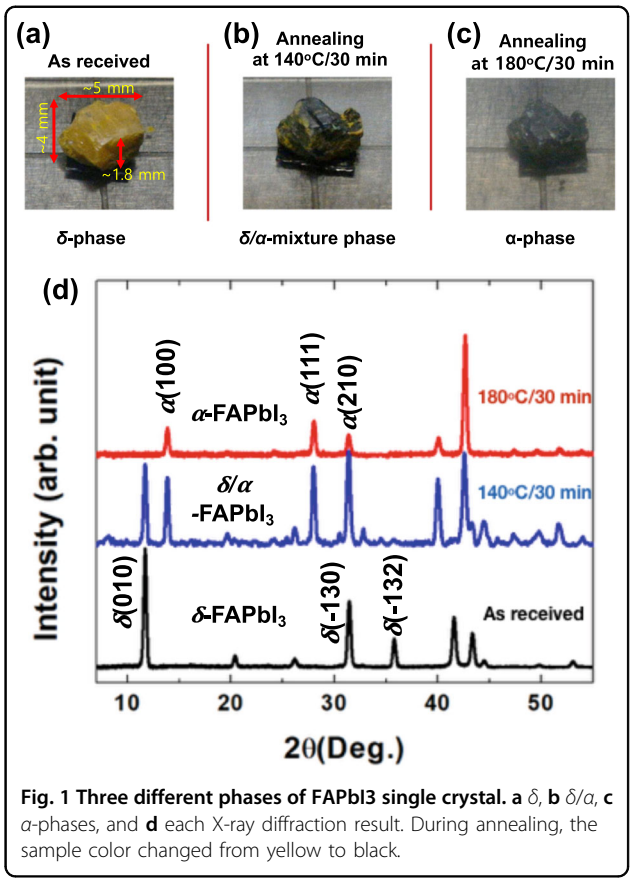

Fig. 1 Three different phases of FAPbI3 single crystal. a δ, **b** δ/α, **c** α-phases, and **d** each X-ray diffraction result. During annealing, the sample color changed from yellow to black.

reflection mode THz-TDS system given that the SC perovskite is a high-absorbing material and that its thickness is not precisely controllable in our fabrication method. We used a typical THz-TDS system with a femtosecond laser. THz pulses were generated in a *p*-InAs crystal pumped with 800 nm central wavelength mode-locked Ti: sapphire (Tsunami, Spectra-Physics) that had a pulse width of 80 *fs* and a repetition rate of 80 MHz. The THz signals were guided by three metal mirrors and silicon beam splitters and focused on the bottom surface of the sample by a TPX lens. Despite the loss of approximately 75% of the signal amplitude, a normal angle of incidence was used to extract accurate complex conductivities[32]. The photoconductive antenna detected the THz signal with a signal-to-noise ratio of 1:5000 in the spectral range from 0.2 to 3.5 THz. In the reflection geometry, the reflected signal from the gold-coated planar mirror was used as a reference, and the extracted conductivities were analyzed by comparing the amplitude ratios and the phase shifts to the signal reflected from the $FAPbI_3$ SC[32]. We placed the reference gold-coated mirror and the $FAPbI_3$ SC horizontally at the top of the system and fixed them firmly to reduce the difference in the position between the reference and the sample, which could cause an additional relative phase shift[33]. The surface of the $FAPbI_3$ was cleaved and sanded flat. To change the phase of the $FAPbI_3$, annealing was used up to 140 °C for 30 min and up to 180 °C for 30 min. The measured time-domain THz signal and optical reflectivity spectra are shown in Supplementary Fig. S1 in the Supplementary Materials.

Their geometrical optimization was performed according to calculations based on first principles according to density functional theory[34] as implemented in the Vienna ab initio simulation package (VASP)[35,36]. The projector augmented wave potentials[37,38] were used to describe the valence electrons, and the exchange-correlation functional was treated by the generalized gradient approximation of Perdew–Burke–Ernzerhof[39] with the DFT-D3[40] van der Waals correction. The wavefunctions were expanded on a plane-wave basis with a kinetic energy cutoff of 500 eV. Geometric relaxation was performed until all forces felt by each atom reached less than 0.01 eV/Å. The Brillouin zone was sampled with the use of $4 \times 4 \times 4$, $8 \times 8 \times 8$, and $2 \times 2 \times 1$ k-point grids for δ-, α-, and their mixed phases, respectively.

For these optimized structures, we calculated their phonon dispersion relations either by using the finite displacement (FD) method[41] or the temperature-dependent effective potential (TDEP) approach[42–44] to properly describe their vibrational properties at room temperature. For the δ- and mixed phases, we used the FD approach given that the FA molecules are relatively stationary in both phases. We used $2 \times 2 \times 2$ and $2 \times 2 \times 1$ supercell structures for the δ- and mixed phases, respectively. For the TDEP approach applied to the α-phase, we performed molecular dynamics (MD) simulations for 160,000 time steps of 1 fs within the canonical ensemble with a constant temperature of 400 K to obtain the converged finite-temperature force constant matrix (FTFCM)[45,46]. The FTFCM was fitted based on considerations of all the forces and displacements between any two atoms at every time step. In the MD simulations, we used a $2 \times 2 \times 2$ supercell structure to properly describe a free rotation of the FA molecules as well as long-range vibration modes. The reduced Brillouin zone was sampled only at the Γ point.

Finally, we produced the THz absorption spectra by computing the THz absorption intensity $I_{\mathrm{THz}}(\nu)$ as a function of the phonon mode ν from the Born effective charge tensor Z^* and the phonon eigenvectors $u_n(\nu)$ of the nth atom evaluated at the Γ point using the relation[47] of

$$I_{\mathrm{THz}}(\nu) \propto \sum_{i=1}^{3} \left| \sum_{n=1}^{N} \sum_{j=1}^{3} Z_{ij}^{*} \frac{u_{nj}(\nu)}{\sqrt{m_n}} \right|^2 \quad (1)$$

where N is the total number of atoms, i and j denote the Cartesian coordinates, and m_n is the mass of the nth atom. To mimic the realistic frequency dependence, a simple Gaussian convolution with a width of 5 THz was used. The partial contributions of the δ- and α-sectors embedded in the mixed phase to the total THz absorption were estimated by running partial summations over $n \in \delta$ and $n \in \alpha$ in Eq. (1).

Results and discussion

Three different phases, the δ-, δ/α-mixed-, and α-phases, were formed by annealing the prepared $FAPbI_3$ SC (Fig. 1a–c). A change in the sample color from yellow to black was clearly observed. From the XRD measurements, all the treated samples were confirmed to have atomic structures of the δ-, δ/α-mixed-, or α-phases (Fig. 1d). These observations were perfectly consistent[28]. We inferred that the δ/α-mixed sample was composed of the δ- and α-phases without any seamed interfaces because no noticeably different structure was observed in the XRD.

During the post-annealing period, the surface morphology of the $FAPbI_3$ SC was also changed (Fig. 2a–c). The as-received sample with the δ-phase exhibited a flat surface. In the δ/α-mixed sample, however, we observed pinholes and separation of a physical structure owing to the different lattice constants[28] (Fig. 2b). The surface roughness dramatically increased in the α-phase sample (Fig. 2c).

To confirm the chemical states of each phase, we performed an X-ray photoelectron spectroscopy (XPS) experiment. The valence edges were changed by 1.94, 1.34, and 1.40 eV at each phase (Fig. 2d). Additionally, the peak positions of N 2*s*, N-C hybridization, and C 2*s* were

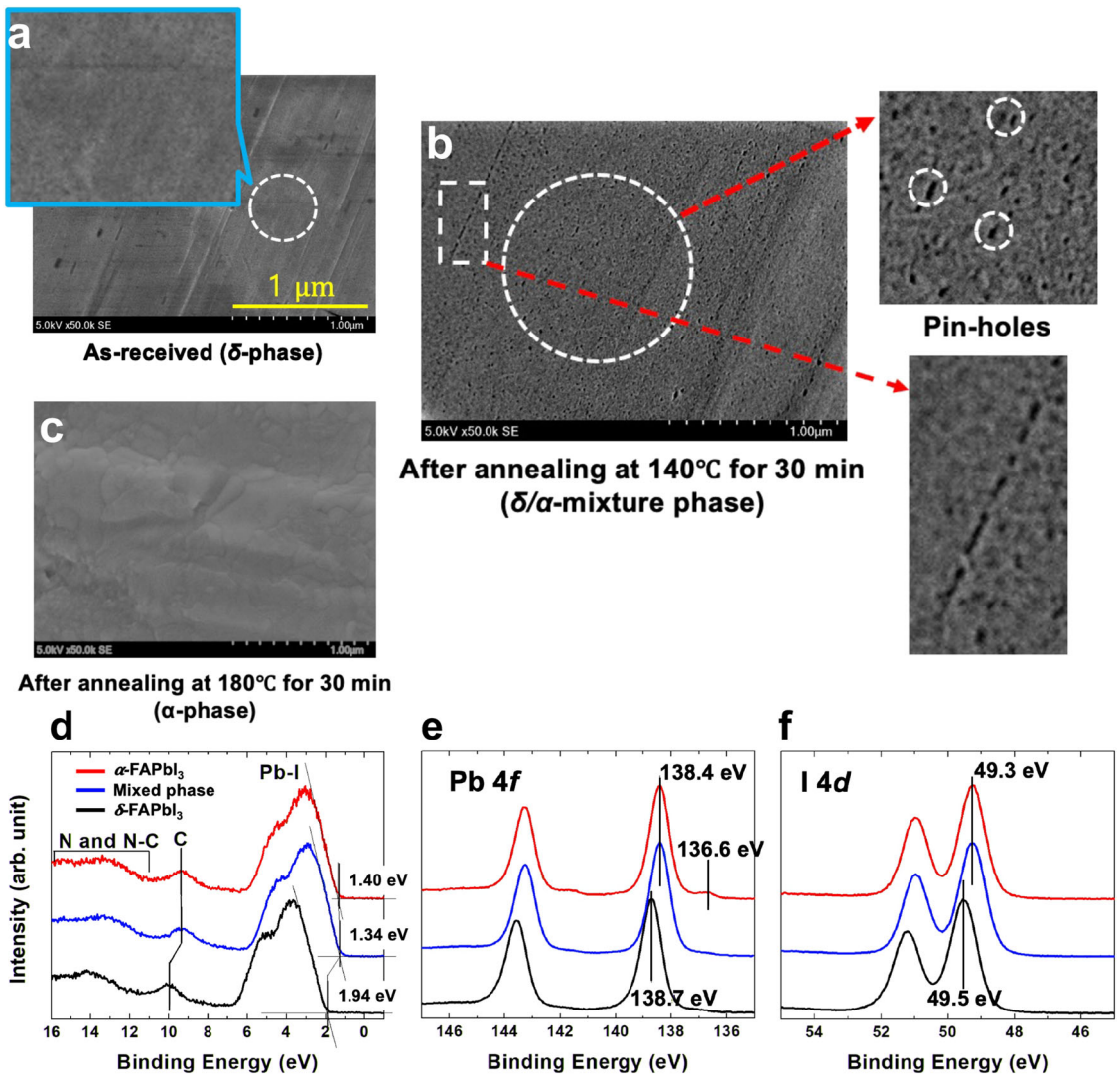

Fig. 2 Basic characterizations for each phase. Surface morphologies, valence, and core-level spectra (Pb 4*f* and I 4*d*) of the **a** *δ*, **b** *δ*/*α*, **c** *α*-phases, respectively.

shifted to low binding energies (Fig. 2d). Interestingly, the Pb $4f_{7/2}$ (138.4 eV) and I $4d_{5/2}$ (49.3 eV) core levels of the *δ*- and *δ*/*α*-mixed-phase samples were not changed (Fig. 2e, f). The chemical state of Pb $4f_{7/2}$ at 136.6 eV in the *α*-phase sample was attributed to the remaining Pb^{0+} metal because of the molecular depletion on the surface caused by postannealing[9,12,13] (Fig. 2e). From these results, we confirmed that there were no new chemical states during post-annealing, even with the dramatic change in surface morphology[48]. This was consistent with the XRD results (Fig. 1d).

We used reflection THz-TDS spectroscopy as a contactless conductivity probe; this technique has been used previously to study the phonon modes of perovskite materials[11,21]. The real conductivities of $FAPbI_3$ SC were measured during the phase transition processes. The annealing changed the synthesized *δ*-phase sample to the *α*-phase through the *δ*/*α*-mixed-phase. Figure 3a shows the real conductivities of the *δ*-, *δ*/*α*-mixed-, and *α*-phase samples extracted with the use of a comparison equation of the sample and reference spectra[32]. Additionally, we performed curve fittings with the use of the Lorentzian harmonic oscillator (LHO) model to find the differences in resonance frequency followed by the phase of $FAPbI_3$. The complex conductivity of the LHO is expressed by

$$\tilde{\sigma}(\omega) = -i \in_0 w(\in_\infty -1) + \sum_j \frac{\in_0 \Omega_j^2 \omega}{i(\omega_{0j}^2 - \omega^2) + \omega\gamma_j} \qquad (2)$$

where ω_{0j}, Ω_j, and γ_j are the resonant frequency, oscillator strength, and scattering rate of the *j*th oscillator,

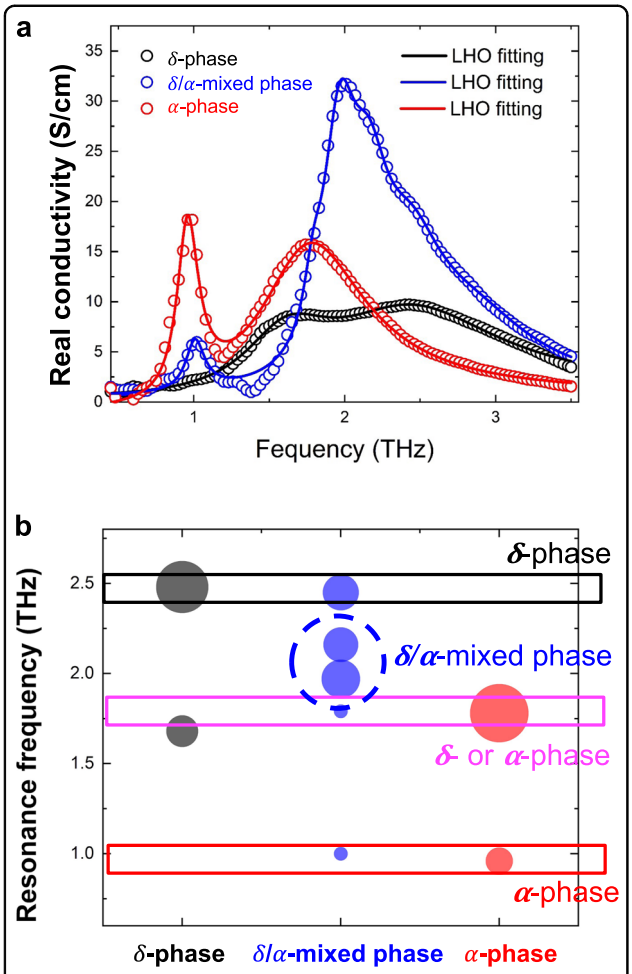

Fig. 3 THz-wave absorption properties. a Real conductivities of the δ-, δ/α-, and α-phase $FAPbI_3$ SC measured by THz-TDS. Circles: measured data, solid lines: Lorentz harmonic oscillator model fitting lines (Table 1). **b** Resonance frequency and oscillator strength of the Lorentzian parameter. The size of the dot is proportional to the oscillator strength of the Lorentzian parameter.

respectively[49]. The resonant frequency, oscillator strength, and scattering rate derived from each phase of $FAPbI_3$ are summarized in Table 1.

For the α-phase sample, we could find indexed peaks at 1 and 1.8 THz related to the Pb-I-Pb transverse vibration and Pb-I longitudinal optical vibration[48,49]. Conversely, the Pb-I-Pb angle vibration was not shown in the δ-phase sample, and the other clear resonance appeared. The most interesting aspect pertains to the fact that the strong resonance absorption peaks of 2.0 and 2.2 THz not present in the δ- and α-phase samples were observed in the δ/α-phase sample.

To investigate the origin of this strong THz absorption observed not only in the δ- and α-phases but also in the mixed phase, we performed first-principle calculations based on density functional theory. Note that the

Table 1 Lorentzian parameters to describe THz conductivity for each phase.

Phase	$\omega_{0j}/2\pi$ (THz)	$\Omega_j/2\pi$ (THz)	$\gamma_j/2\pi$ (THz)
δ-phase	1.7	2.7	0.7
	2.5	4.4	1.4
δ/α-mixed phases	1.0	1.2	0.2
	1.8	1.2	0.2
	2.0	3.3	0.3
	2.2	2.9	0.3
	2.5	3.0	0.5
α-phase	1.0	2.3	0.2
	1.8	4.9	0.9

experimentally observed THz absorption spectra of the δ- and α-phases were completely different from each other and that the mixed phase exhibited a completely distinct THz spectrum that was not directly expected from those of the two unmixed phases. From such unexpected observations, we could assume that there was a significant structural modification from the structure of the unmixed phases during the mixing process. However, our XRD measurements did not provide any other peaks that were distinguishable from those observed in the original δ- and α-phases, implying no noticeable structural deformation even near the interfaces between the two phases.

To evaluate our XRD measurements, we constructed the model structures of the two unmixed phases and the mixed phase. The crystal structures of δ- and α-$FAPbI_3$ formed hexagonal and cubic unit cells with calculated equilibrium lattice constants of $a_\delta = 9.021$ Å, $c_\delta = 7.753$ Å, and $a_\alpha = 6.398$ Å (Fig. 4a, b). The model structure of the mixed phase formed a superlattice-like configuration of the δ- and α-phases along the [0001] direction of the hexagonal lattice with interfaces that connected the two displayed phases. Specifically, the model mixed phase was constructed by combining a $\sqrt{2} \times \sqrt{2} \times 3$ supercell of α-$FAPbI_3$ and a $1 \times 1 \times 3$ supercell of δ-$FAPbI_3$. The in-plane and out-of-plane lattice constants of the mixed phase were selected to be $a = \sqrt{2}a_\alpha$ and c = 44.689 Å, yielding the minimum total energy. We did not find any noticeable change in the lattice spacing in the model interface structure given that the in-plane lattice mismatch between the two composed unmixed phases was less than 1%. This guaranteed a very stable interface structure without any dangling bonds, while essentially the same chemical bonds as those that existed in the unmixed phases were maintained. We confirmed that this model interface structure was consistent with our XRD measurements.

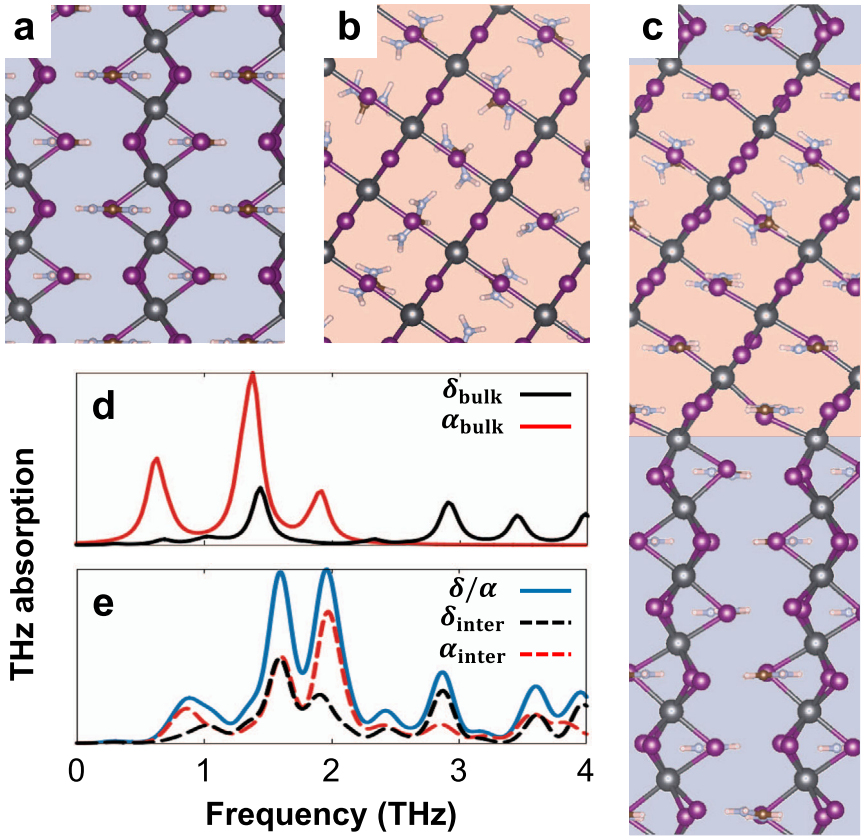

Fig. 4 Theoretical simulations. Side view of schematic crystal structures for the **a** δ- and **b** α-$FAPbI_3$ phases and **c** the mixed phase. The Pb, I, C, N, and H atoms comprising $FAPbI_3$ are denoted by dark gray, purple, brown, sky blue, and pink balls, respectively, and blue and red shadows indicate the δ- and α-phases, respectively. Calculated THz absorption spectra of the **d** bulk phase of α- (α_{bulk}, red solid line) and δ-$FAPbI_3$ (δ_{bulk}, black solid line) and (e) the mixed phase (δ/α, blue solid line). In **e**, we represent the contributions of the local α- (α_{inter}, red dashed line) and δ-phases (δ_{inter}, black dashed line) to the total absorption spectrum.

Using the structures of the two unmixed phases and the model mixed phase illustrated in Fig. 4a–c, we evaluated their phonon dispersion relations based on the application of the methods described in the "Methods" section and the Supplementary Note in the Supplementary Materials. The calculated phonon relations of the three phases, which are shown in Supplementary Fig. S2 in the Supplementary Materials, were used together with their Born effective charge tensors to evaluate the THz absorption spectra. Figure 4d shows the volume-normalized THz absorption spectra of the two unmixed phases. The absorption spectrum of the δ-$FAPbI_3$ was much weaker than that of the α-phase and was consistent with our experimentally observed spectra shown in Fig. 3a. Specifically, for α-$FAPbI_3$, we found three strong THz absorption peaks near $\nu = 0.65$, 1.4, and 1.9 THz, similar to those observed in cubic $MAPbBr_3$[10]. These calculated absorption peaks could be matched to the experimentally observed peaks shown in Fig. 3(a). The two first peaks corresponded to each other, whereas the broad second peak near $\nu = 1.8$ THz observed in the experiment could be regarded as being composed of the second and third peaks in the calculation. For δ-$FAPbI_3$, its first and second peaks at approximately $\nu = 1.5$ and 2.9 THz were quite well matched to the experimentally observed first (1.7 THz) and second (2.7 THz) peaks.

If there were no additional infrared (IR)-active phonon vibration modes at the interface, the THz absorption spectrum of the mixture would be similar to the simple addition of the spectra of the α- and δ-phases. However, we experimentally observed strong and unexpected THz absorption peaks in the mixed phase. Interestingly, our calculation also produced novel THz absorption peaks that originated from interfacial phonon vibration modes in the mixed phase, as shown in Fig. 4e. We observed two strong absorption peaks near $\nu = 1.6$ and 1.95 THz that were clearly distinguishable from those of the α- and δ-phases (Fig. 4d) and assigned them to the two experimentally observed peaks at 2.0 and 2.2 THz. To further explore the origin of these two unexpected absorption peaks, we evaluated the partial contributions of the α- and δ-sectors embedded in the interface to the total THz

absorption. As displayed in Fig. 4e with dashed lines, both sectors contributed to the first peak and indicated the simultaneous vibrations of both the α-and δ-sectors, whereas the second peak was mainly composed of the optical vibration of the α-sector embedded in the interface. These vibrational motions can be observed in the form of animations (see the Supplementary Information).

Conclusion

In conclusion, $FAPbI_3$ SCs of three different phases, the δ-, δ/α-mixed-, and α-phases, were prepared to investigate their phonon vibrational characteristics. In the δ/α-mixed-phase sample, which simply consisted of physical additions of the δ- and α-phases without any new chemical states, we observed unusual THz-wave absorption peaks at 2.0 and 2.2 THz that were not related to the phonon modes originating from the δ- and α-phases. We revealed that these unusual THz-wave absorptions originated from the interfacial phonon vibration modes in the mixed phase, which was a seamlessly combination of the δ- and α-phases of $FAPbI_3$. This unusual THz-wave absorption may provide new possibilities for exploring OHP-based THz-based applications.

Acknowledgements

This work was supported by funding from the 2020 research grant program of Izumi Zaidan (Japan). We gratefully acknowledge the financial support from the Korean Ministry of Science and ICT through the National Research Foundation (NRF) of Korea (NRF-2019R1A2C1005417). This work was also supported by the Basic Science Research Program (NRF-2020R1C1C1013646) through the NRF funded by the Korean Ministry of Education. This research was partially financially supported by the Australian Research Council (ARC) through the Discovery, DECRA Fellowship, and Laureate Fellowship programs. Some portion of our computational work was done using the resources of the KISTI Supercomputing Center (KSC-2020-CRE-0011).

Author details

[1]YUHS-KRIBB, Medical Convergence Research Institute, College of Medicine, Yonsei University, Seoul, Republic of Korea. [2]Department of Physics, Kyung Hee University, Seoul, Republic of Korea. [3]School of Chemical Engineering and Australian Institute for Bioengineering and Nanotechnology (AIBN), University of Queensland, St Lucia, QLD, Australia. [4]Division of Materials Science, Nara Institute of Science and Technology, Ikoma, Nara, Japan. [5]Department of Information Display and Research Institute for Basic Sciences, Kyung Hee University, Seoul, Republic of Korea. [6]Division of Materials Science, Faculty of Pure and Applied Sciences, University of Tsukuba, Ibaraki, Japan

Conflict of interest

The authors declare no competing interests.

Supplementary information The online version contains supplementary material available at https://doi.org/10.1038/s41427-021-00343-7.

Received: 5 August 2021 Revised: 30 September 2021 Accepted: 4 October 2021
Published online: 26 November 2021

References

1. Park, N. G., Grätzel, M. & Miyasaka, T. *Organic-Inorganic Halide Perovskite Photovoltaics: From Fundamentals to Device Architectures* (Springer, 2016).
2. Telychko, M. & Lu, J. Recent advances in atomic imaging of organic-inorganic hybrid perovskites. *Nano Mater. Sci.* **1**, 260–267 (2019).
3. DeQuilettes, D. W. et al. Photo-induced halide redistribution in organic-inorganic perovskite films. *Nat. Commun.* **7**, 11683 (2016).
4. Yi, Z. et al. Will organic-inorganic hybrid halide lead perovskites be eliminated from optoelectronic applications? *Nanoscale Adv.* **1**, 1276–1289 (2019).
5. Kagan, C. R., Mitzi, D. B. & Dimitrakopoulos, C. D. Organic-inorganic hybrid materials as semiconducting channels in thin- film field-effect transistors. *Science* **286**, 945–947 (1999).
6. Maeng, I. et al. Significant THz absorption in CH_3NH_2 molecular defect-incorporated organic-inorganic hybrid perovskite thin film. *Sci. Rep.* **9**, 5811 (2019).
7. Zhang, Y. et al. Halide perovskite single crystals: optoelectronic applications and strategical approaches. *Energies* **13**, 4250 (2020).
8. Yoo, E. J. et al. Resistive switching behavior in organic-inorganic hybrid $CH_3NH_3PbI_{3-x}Cl_x$ perovskite for resistive random access memory devices. *Adv. Mater.* **27**, 6170–6175 (2015).
9. Maeng, I. et al. Unique phonon modes of a $CH_3NH_3PbBr_3$ hybrid perovskite film without the influence of defect structures: an attempt toward a novel THz-based application. *NPG Asia Mater.* **12**, 1–7 (2020).
10. Snaith, H. Perovskites: the emergence of a new era for low-cost, high-efficiency solar cells. *J. Phys. Chem. Lett.* **4**, 3623–3630 (2013).
11. Maeng, I. et al. Strong linear correlation between CH_3NH_2 molecular defect and THz-wave absorption in $CH_3NH_3PbI_3$ hybrid perovskite thin film. *Nanomaterials* **10**, 721 (2020).
12. Jung, M.-C. et al. Formation of CH_3NH_2-incorporated intermediate state in $CH_3NH_3PbI_3$ hybrid perovskite thin film formed by sequential vacuum evaporation. *Appl. Phys. Express* **12**, 015501–015501 (2018).
13. Lee, Y. M. et al. Significant THz-wave absorption property in mixed δ- and α-$FAPbI_3$ Hybrid perovskite flexible thin film formed by sequential vacuum evaporation. *Appl. Phys. Express* **12**, 051003 (2019).
14. Sendner, M. et al. Optical phonons in methylammonium lead halide perovskites and implications for charge transport. *Mater. Horiz.* **3**, 613–620 (2016).
15. Zhao, D. et al. Low-frequency optical phonon modes and carrier mobility in the halide perovskite $CH_3NH_3PbBr_3$ using terahertz time-domain spectroscopy. *Appl. Phys. Lett.* **111**, 201903 (2017).
16. Hashimshony, D. et al. Characterization of the electrical properties and thickness of thin epitaxial semiconductor layers by THz reflection spectroscopy. *J. Appl. Phys.* **90**, 5778–5781 (2001).
17. Song, H. J. & Nagatsuma, T. Present and future of terahertz communications. *IEEE Trans. Terahertz Sci. Technol.* **1**, 256–263 (2011).
18. Spies, J. A. et al. Terahertz spectroscopy of emerging materials. *J. Phys. Chem. C* **124**, 22335–22346 (2020).
19. Tonouchi, M. Cutting-edge terahertz technology. *Nat. Photonics* **1**, 97–105 (2007).
20. Davies, C. L. et al. Impact of the organic cation on the optoelectronic properties of formamidinium lead triiodide. *J. Phys. Chem. Lett.* **9**, 4502–4511 (2018).
21. La-O-Vorakiat, C. et al. Phonon mode transformation across the orthohombic-tetragonal phase transition in a lead iodide perovskite $CH_3NH_3PbI_3$: a terahertz time-domain spectroscopy approach. *J. Phys. Chem. Lett.* **7**, 1–6 (2016).
22. Frost, J. M. & A. Walsh, A. *Organic-Inorganic Halide Perovskite Photovoltaics: From Fundamentals to Device Architectures* 1–17 (Springer International Publishing, 2016).
23. Ho, L., Pepper, M. & Taday, P. Terahertz spectroscopy: signatures and fingerprints. *Nat. Photonics* **2**, 541–543 (2008).
24. Jeon, T. I. & Grischkowsky, D. Characterization of optically dense, doped semiconductors by reflection THz time domain spectroscopy. *Appl. Phys. Lett.* **72**, 3032–3034 (1998).
25. Kim, H. et al. Direct observation of mode-specific phonon-band gap coupling in methylammonium lead halide perovskites. *Nat. Commun.* **8**, 687 (2017).
26. Nagai, M. et al. Longitudinal optical phonons modified by organic molecular cation motions in organic-inorganic hybrid perovskites. *Phys. Rev. Lett.* **121**, 145506 (2018).
27. Straus, D. B. & Kagan, C. R. Electrons, excitons, and phonons in two-dimensional hybrid perovskites: connecting structural, optical, and electronic properties. *J. Phys. Chem. Lett.* **9**, 1434–1447 (2018).

28. Han, Q. et al. Single crystal formamidinium lead iodide ($FAPbI_3$): insight into the structural, optical, and electrical properties. *Adv. Mater.* **28**, 2253–2258 (2016).
29. Rothmann, U. M. et al. Atomic-scale microstructure of metal halide perovskite. *Science* **370**, 548 (2020).
30. Cordero, F. et al. Stability of cubic $FAPbI_3$ from X-ray diffraction, anelastic, and dielectric measurements. *J. Phys. Chem. Lett.* **10**, 2463–2469 (2019).
31. Wagner, C. D., Riggs, W. M., Davis, L. E., Moulder, J. F. & Muilenberg, G. E. *Handbook of X-ray Photoelectron Spectroscopy: A Reference Book of Standard Spectra for Identification and Interpretation of XPS Data - Catalog - UW-Madison Libraries* (1995).
32. Brunner, F. D. J., Schneider, A. & Günter, P. A terahertz time-domain spectrometer for simultaneous transmission and reflection measurements at normal incidence. *Opt. Express* **17**, 20684 (2009).
33. Nashima, S., Morikawa, O., Takata, K. & Hangyo, M. Measurement of optical properties of highly doped silicon by terahertz time domain reflection spectroscopy. *Appl. Phys. Lett.* **79**, 3923–3925 (2001).
34. Kohn, W. & Sham, L. J. Self-consistent equations including exchange and correlation effects. *Phys. Rev.* **140**, A1133 (1965).
35. Kresse, G. & Hafner, J. Ab initio molecular dynamics for liquid metals. *Phys. Rev. B* **47**, 558–561 (1993).
36. Kresse, G. & Furthmüller, J. Efficient iterative schemes for ab initio total-energy calculations using a plane-wave basis set. *Phys. Rev. B Condens. Matter Mater. Phys.* **54**, 11169–11186 (1996).
37. Joubert, D. & Ultrasoft, From Pseudopotentials to the projector augmented-wave method. *Phys. Rev. B Condens. Matter Mater. Phys.* **59**, 1758–1775 (1999).
38. Blöchl, P. E. Projector augmented-wave method. *Phys. Rev. B* **50**, 17953–17979 (1994).
39. Perdew, J. P., Burke, K. & Ernzerhof, M. Generalized gradient approximation made simple. *Phys. Rev. Lett.* **77**, 3865–3868 (1996).
40. Grimme, S., Antony, J., Ehrlich, S. & Krieg, H. A consistent and accurate ab initio parametrization of density functional dispersion correction (DFT-D) for the 94 elements H-Pu. *J. Chem. Phys.* **132**, 154104 (2010).
41. Togo, A. & Tanaka, I. First principles phonon calculations in materials science. *Scr. Mater.* **108**, 1–5 (2015).
42. Hellman, O. & Abrikosov, I. A. Temperature-dependent effective third-order interatomic force constants from first principles. *Phys. Rev. B Condens. Matter Mater. Phys.* **88**, 144301 (2013).
43. Hellman, O., Steneteg, P., Abrikosov, I. A. & Simak, S. I. Temperature dependent effective potential method for accurate free energy calculations of solids. *Phys. Rev. B Condens. Matter Mater. Phys.* **87**, 104111 (2013).
44. Hellman, O., Abrikosov, I. A. & Simak, S. I. Lattice dynamics of anharmonic solids from first principles. *Phys. Rev. B Condens. Matter Mater. Phys.* **84**, 180301 (2011).
45. Hoover, W. G. Canonical dynamics: equilibrium phase-space distributions. *Phys. Rev. A* **31**, 1695–1697 (1985).
46. Nosé, S. A molecular dynamics method for simulations in the canonical ensemble. *Mol. Phys.* **52**, 255–268 (1984).
47. Skelton, J. M. et al. Lattice dynamics of the tin sulphides SnS2, SnS and Sn2S3: vibrational spectra and thermal transport. *Phys. Chem. Chem. Phys.* **19**, 12452–12465 (2017).
48. Davies, C. L. et al. Impact of the organic cation on the optoelectronic properties of formamidinium lead triiodide. *J. Phys. Chem. Lett.* **9**, 4502–4511 (2018).
49. Grechko, M., Bretschneider, S. A., Vietze, L., Kim, H. & Bonn, M. Vibrational coupling between organic and inorganic sublattices of hybrid perovskites. *Angew. Chem. Int. Ed.* **57**, 13657–13661 (2018).